Static stress drop associated with brittle slip events on exhumed faults

W.A. Griffith[1], G. Di Toro[2], G. Pennacchioni[2], D.D. Pollard[1], and S. Nielsen[3]
[1] Department of Geological and Environmental Sciences, Stanford University, Stanford, CA
[2] Dipartimento di Geoscienze, Università di Padova, Padova, IT
[3] Istituto Nazionale di Geofisica e Vulcanologia, Roma, IT

Abstract

We estimate the static stress drop on small exhumed strike-slip faults in the Lake Edison granodiorite of the central Sierra Nevada (California). The sub-vertical strike-slip faults were exhumed from 4-15 km depth, and were chosen because they are exposed in outcrop along their entire tip-to-tip lengths of 8-12 m. Slip nucleated on joints and accumulated by ductile shearing (forming quartz mylonites from early quartz vein filling in joints) and successive brittle faulting (forming epidote-bearing cataclasites). The occurrence of thin, < 1 mm wide, pseudotachylytes along some small faults throughout the study area suggests that some portion of the brittle slip was seismic. We suggest that the contribution of seismic slip to the total slip along the studied cataclasite-bearing small faults may be estimated by the length of epidote-filled, rhombohedral dilatational jogs (rhombochasms) distributed semi-periodically along the length of the faults.

The interpretation that slip recorded by rhombochasms occurred in single events is based on evidence that: 1) epidote crystals are randomly oriented and undeformed within the rhombochasm; and 2) cataclasite structure in principal slip zones does not include clasts of previous cataclasite. We thereby constrain *both* the rupture length and slip. Based on these measurements, we calculate stress drops ranging over 90-250 MPa, i.e., one to two orders of magnitude larger than typical seismological estimates for earthquakes, but similar in magnitude to recent observations of small (< M2) earthquakes from the San Andreas Fault Observatory at Depth (SAFOD). These inferred seismic ruptures occurred along small, deep-seated faults, and,

given the calculated stress drops and observations that brittle faults exploited joints sealed by quartz-bearing mylonite, we conclude that these were “strong” faults.

Introduction

Statement of the problem

The static shear stress drop associated with earthquakes is a fundamental quantity that scales linearly with slip, particle velocity and acceleration [*Scholz*, 2002], and is typically calculated using a characteristic source dimension (e.g., fault radius for a circular fault), average slip, and the estimated shear modulus of the host rock. The stress drop ($\Delta\sigma$) is defined as the difference between σ_{zx}^{r}, the peak shear stress in the remote field, and σ_{zx}^{c}, the shear stress resolved on the fault after slip, where slip is in the x direction and z is normal to the fault. *Kanamori* [1994] distinguishes two end-member characteristic faults based on the stress σ_{zx}^{r} at which they fail: (1) *weak* faults for which $\sigma_{zx}^{r} \approx$20MPa; and (2) *strong* faults for which $\sigma_{zx}^{r} \approx$200MPa.

Stress drops measured in triaxial experiments of shear failure of intact rocks are typically on the order of hundreds of MPa to GPa [e.g., *Brace and Byerlee*, 1966]. Triaxial experiments with sawcut samples have yielded slightly smaller stress drops in the range from tens to hundreds of MPa [*Brace and Byerlee*, 1966]. These results indicate that, at least in the laboratory, faults in geomaterials are strong. In both types of experiments, the shear stress drop was a fraction of the peak yield stress; however stress drops on the order of hundreds of MPa in the upper crust would constitute a near total stress drop ($\sigma_{zx}^{c} \approx 0$). Laboratory stress drops stand in stark contrast to seismologically observed stress drops, typically on the order of 0.1-100 MPa, a fraction of the shear strength of intact rock at seismogenic depths [e.g., *Kanamori*, 1994; *Abercrombie*, 1995].

The earthquake rupture process has long been considered to follow a self-similar scaling relationship, as stress drop has been observed to be independent of magnitude [*Aki*, 1967]; however this scale independence has been observed to break down for earthquakes below M_L~3, as small earthquakes appear to be associated with smaller stress drops [e.g., *Archuleta et al*., 1982; *Hanks*, 1982]. Minimum source dimensions on the order of 100 m have been inferred for earthquakes, offering one solution for the apparent deviation in scaling [*Archuleta et al*., 1982, *Guo et al*., 1992]. If 100 m is truly a minimum source dimension (presumably controlled by geometry or nucleation length), then smaller observed moments must be attributed to a lower values of average fault slip leading to smaller calculated stress drops. More recently, however, this breakdown in scaling for small earthquakes has been established to be an artifact of severe near surface attenuation of high frequency waves [e.g., *Hanks*, 1982]. Attenuation of high frequency waves artificially distorts the amplitude spectrum, making interpretation of the corner frequency difficult [e.g., *Hanks*, 1982; *Hough and Anderson*, 1988; *Abercrombie*, 1995; *Prejean and Ellsworth*, 2001].

Researchers have attempted to circumvent the problem of small source resolution by examining data recorded by seismometers closer to the source, in deep boreholes [*Abercrombie*, 1995], or in deep South African gold mines [e.g., *Richardson and Jordan*, 2002]. Recent studies suggest that using borehole seismometers may not effectively alleviate problems with high frequency attenuation [*Ide and Beroza*, 2001; *Imanishi and Ellsworth*, 2006]. Using a stable spectral ratio method to analyze microearthquakes from the San Andreas Fault Observatory at Depth (SAFOD) seismic array in Parkfield, CA, *Imanishi and Ellsworth* [2006] showed that there is no scaling breakdown for stress drop or apparent stress and found that half of the microearthquakes examined had static stress drops greater than 10 MPa.

An alternative approach to studying the source of small earthquakes, which effectively removes any spatial ambiguity introduced by inferring earthquake source dimensions, is to study the earthquake source by direct examination of ancient earthquake ruptures along faults exhumed from hypocentral depths. Detailed investigation of faults at the outcrop and microscopic scale can resolve to high precision the spatial extent and geometry of rupture in two dimensions and the fault slip. Given these parameters and the shear modulus of the fault host rocks the stress drop can be calculated with the same elastic dislocation models commonly employed by earthquake seismologists. Unfortunately, such estimates have been difficult to come by because a number of factors need to be present in outcrop to successfully estimate the stress drop:

1) The fault must be exposed along its entire length in order to measure the source dimension, and the fault must be isolated from nearby faults to lessen the potential for fault interaction;
2) Slip must be measured for a single slip event;
3) Evidence of seismic slip must be present if the slip is interpreted to be related to ancient earthquakes. For exhumed faults, this means that pseudotachylyte (solidified friction-induced melts produced during seismic slip; *Sibson*, 1975) must be present within the slipping zone [*Cowan*, 1999].

Complete slip distributions have been measured along the entire length of faults exposed at the Earth's surface via remote sensing and field mapping [e.g., *Maerten et al*., 2001; *Manighetti et al*., 2001], and 3D seismic datasets [e.g., *Willemse*, 1997; *Kattenhorn and Pollard*, 2001]. Slip estimates along small exhumed faults most typically consist of sparse (one or two) measurements of piercing points along the fault representing only the relative particle displacement at the point of measurement [e.g., *Shipton et al*., 2006]. With few exceptions [e.g., *Di Toro et al*., 2005], slip measurements along natural faults almost always represent the total accumulated slip (representing multiple slip episodes) during the history of fault activity.

Here we attempt to use geological observations to calculate the stress drops for slip events along small exhumed faults by describing deformation associated with single seismic slip events which can be mapped in two dimensions from one tip of the fault to the other. The results of these calculations are compared to data from the seismological record. This approach effectively removes ambiguity about the source dimensions and geometry inherent in the seismological inverse problem by affording direct observation of the source.

Bear Creek Faults

Fracturing and faulting has been documented in the Bear Creek drainage, in the southern half of the Mount Abbot quadrangle in the Sierra Nevada batholith [e.g., *Lockwood and Lydon*, 1975; *Segall and Pollard*, 1983a, 1983b; *Martel et al*., 1988]. These studies have concentrated on the Lake Edison Granodiorite (~88 Ma) whose depth of emplacement is estimated at 4-15 km based on amphibole geobarometry [*Ague and Brimhall*, 1988]. K-Ar ages from muscovite in the fractures date the Bear Creek faults at 79 Ma, and these faults have been interpreted as having grown soon after pluton emplacement [*Segall et al*., 1990].

Post-magmatic structures in Bear Creek include nearly vertical joints and faults [e.g., *Segall and Pollard*, 1983*a*, 1983*b*; *Martel et al*., 1988]. Initial fracturing produced a single set of joints (Figure 1I) striking predominantly ENE [Segall and Pollard, 1983a; Martel et al., 1988]. Subsequent crystal-plastic shearing localized on the joints, producing quartz (from former quartz veins filling the joints) and granodiorite mylonites (Figure 1II, A). As pluton cooling progressed, cataclasis became the dominant deformation mechanism. Brittle slip localized on the boundaries between tabular quartz mylonites and host granodiorites (Figure 1II-III, B). *Griffith et al*. [2008]

showed that some of these brittle slip zones are associated with thin (<300 μm), discontinuous pseudotachylyte veins (Figure 1II-III, C). The pseudotachylytes are typically found in small patches in narrow (< 200 μm) slip zones where cataclasite is either poorly developed or completely absent [*Griffith et al*., 2008]. This observation suggests that pseudotachylyte was either not formed in thicker (>200 μm) cataclasite slip zones due to distributed shear (and thus broadened frictional heat generation), or were poorly preserved due to enhanced permeability of the thicker granular cataclasite during exhumation. The presence of pseudotachylyte veins along the Bear Creek faults suggests that these faults were seismic during the brittle phase of their evolution.

Rhombochasms

Field Observations

The Bear Creek small faults are commonly associated with epidote veins in extensional domains along the faults (Figure 2), as for example: (1) at releasing bends along faults (Figure 2A); (2) where two fault segments link in dilational steps (e.g. left step for left-lateral faults; Figure 2B); and (3) at fault tips as extensional splays [*Segall and Pollard*, 1983a]. A fourth structure, distinctly different from the former three, occurs where the cataclastic slip zone jumps from one side of a quartz mylonite to the other (Figure 2C). In this latter case the veins have a typical rhomboidal shape and are referred to as *rhombochasms* throughout the following sections. Where rhombochasms are present, they are often distributed semi-periodically along a fault (Figure 3). The rhombochasms and the epidote-veins are often associated with bleached halos in the adjacent host rock (Figure 2A-C), a result of plagioclase and biotite alteration to saussurite and chlorite, respectively. In outcrops orthogonal to faults and parallel to the fault slickenlines (approximately the case in the Bear Creek subhorizontal outcrops) the length of rhombochasms sides that are parallel to the fault provide a direct estimate of the fault slip as the rhombochasm formed (e.g., Figure 3).

Minerals in the rhombochasms typically appear to be uniform in color and texture (prismatic epidote grains with no apparent preferred orientation, and minor chlorite). In some cases epidote are interspersed with brecciated subangular clasts of quartz and the host granodiorite (Figure 2C) resembling implosion breccias [*Sibson*, 1985; 1986].

Microstructural Observations

Rhombochasms are filled principally with randomly oriented columnar (~0.1 to 2.5 mm in length) epidote and variably with chlorite embedding subangular quartz clasts (Figure 4A-C). The vein microstructure indicates growth in an open fluid-filled cavity without evidence of incremental growth by the crack-seal mechanism [*Ramsay*, 1980] (Figure 4A). Crystals are not deformed or broken (Figure 4C). Slip zones (generally <1mm thick) entering and departing on the opposite sides of the rhombochasm (Figure 4B) are always left-stepped, switching from the one boundary between quartz vein and host granodiorite to the other, consistent with the left-lateral sense of shear. Rhombochasms along the same fault consistently show the same stepping asymmetry. We interpret this observation to mean that the length of each rhombochasm approximates the brittle slip magnitude that occurred at the corresponding position along the fault.

In some cases, thin (<200 μm), veins outline the slip zones and extend partly into the rhombochasms (Figure 4B, D). In Figure 4B, these veins overlap the rhombochasm by approximately 9 mm along the northeast boundary and approximately 5 mm on the southwest boundary. Thin epidote veins on the upper left and lower right corners of rhombochasms also extend for a short distance (a few cm) along the granodiorite-mylonite interface, but these terminate at the rhombochasm opening (Figure 4B). The typical rhombochasm boundary is knife-edged with no cataclasis of the host rock or the minerals in the rhombochasm at the boundary (Figure 4E), whereas slip zones that penetrate into the rhombochasm form a contact between undeformed rhombochasm mineral fillings and the host granodiorite. In some places, slip zones penetrating into rhombochasms can be seen to truncate clasts within the rhombochasm, while these slip zones are truncated at their tips by undeformed epidote crystals, suggesting that rhombochasm mineral infilling was synchronous with slip (Figure 4F). In other cases the slip zone terminates at the rhombochasm opening (Figure 4G).

Conceptual Model

The component of brittle slip along small faults resulting in cataclasite formation may be distinguished from the slip contribution from previous ductile shearing because epidote-filled, rhombohedron-shaped dilational jogs opened at bends and step-overs during brittle slip, and are distributed along the length of the faults. We argue that brittle slip occurred along the measured fault lengths in single slip events. Epidote crystals are randomly oriented and undeformed within the rhombochasms (Figure 4C). The epidotes were not broken after initial opening and precipitation as should be expected if the rhombochasms opened incrementally, as epidote precipitation was coincident with slip along the faults. Also, some small faults in the Bear Creek area contain pseudotachylytes [*Griffith et al.*, 2008] suggesting that seismic slip occurred during brittle deformation along these faults. However, as previously noted, pseudotachylytes are only developed (or preserved) locally along small faults and tend to be absent in cataclasite slip zones thicker than ~ 200 μm [*Griffith et al.*, 2008]. Because cataclasites along these faults are consistently thicker than 200 μm, we should not expect to see pseudotachylyte if our previous observations are predictive. However pseudotachylytes described by Griffith et al., 2008 do show common static overgrowths of epidote. This suggests that the rhombochasm-bearing small faults investigated in this study may also have developed during the same ambient conditions as the pseudotachylyte-bearing faults, and is evidence that the the rhombochasm-bearing faults may also have been seismic. In some places rhombochasms contain breccias resembling implosion breccias [e.g., *Sibson*, 1985; *Sibson*, 1986] that also point toward a fast rate of deformation. Slickenlines on faults commonly plunge less than 15^{o} on studied faults and the offset measured from the rhombohedron lengths on subhorizontal outcrop should underestimate the actual slip by at most 4% (error = $1-\cos 15^{o}$).

The unique combination of factors listed above distinguishes these observations from previous attempts to estimate coseismic parameters such as stress drop from exhumed faults because we can constrain *both* the rupture length and slip [e.g., *Sibson*, 1975; *Di Toro et al.*, 2005].

Slip Distributions

Figure 3 shows the profiles of four small faults in the Bear Creek area exposed along their entire lengths, ranging from 8 to 12 m. We measured the total slip (from aplite dike offset) and the distributions of rhombochasm lengths for two faults, the Bear Creek Meadows Fault (BCMF) and the Upper Hilgard Fault (UHF) (Figure 5).

The BCMF consist of an en-echelon array of highly overlapping, right-stepping fault segments. We estimated brittle slip using seven rhombochasms distributed along the central segment (Figure 3, BCMF). No hard linkage was observed along the overlapping echelon segments on BCMF, nor was any macroscopic evidence evident for brittle reactivation of the mylonite fracture fillings on these segments overlapping the central one. The zero slip data points on either side of the slip distribution (Figure 5A) correspond to the tips of the central fault segment. Rhombochasms occur within the data gaps (e.g. position ranges 590-770 cm and 870-1350 cm), but they were too complicated in shape to use as slip markers. The presence of rhombochasms along the length of the BCMF does indicate that brittle slip occurred along the entire length of the fault segment; therefore the measured length of the fault segment accurately represents the source dimension. The slip maximum occurs slightly west of center and appears to taper toward the fault tips. The average measured brittle slip on the fault is 2.1 cm.

The UHF consists of two hard-linked fault segments (i.e. the fault segments are linked by fractures across the relay zone). In the case of the UHF, only the easternmost fault tip is exposed. The westernmost fault tip is buried under debris. This debris cover is approximately 2-3 m wide, and the fault does not continue on the other side. Near the debris cover, splay cracks are concentrated on the southern side of the fault. These two observations suggest that the fault length is no more than a couple of meters greater than the visible length. Rhombochasms are distributed more evenly than in the BCMF, therefore the slip distribution is more clearly discernable (Figure 5B). The slip distribution appears to be flat along most of the fault and tapers sharply at the western end. Slip tapers more gently on each segment in the relay zone. The average measured brittle slip on the UHF is 2.0 cm.

As suggested previously, the rhombochasm length distribution measured from outcrop maps should closely approximate the brittle slip distribution, and possibly the seismic slip distribution, along these faults. The observed offset of an aplite dike on the BCMF is approximately 35 cm, while that measured along the UHF is 42 cm. Both of these are significantly greater than the measured brittle slips. This gives us an indirect way to estimate the ductile (i.e., crystal-plastic shear of quartz) contribution to slip. The discrepancy between brittle slip and total slip should approximate the offset from ductile shearing of the tabular quartz mylonites extending much of the length of the faults.

Stress Drop

The constant stress drop model used to calculate the stress drops of ruptures on the rhombochasm-bearing Bear Creek faults, and in many seismological models [e.g., *Kanamori and Anderson*, 1975], is a special case of the *Eshelby* [1957] analytical solution for the elastic field of an ellipsoidal inclusion. The circular "penny-shaped crack" model assumes that the principal ellipsoidal axis c is much smaller than the other principal axes, a and b (Figure 6). If the elliptical fault can be approximated as a circle ($a = b$) the slip distribution is given by [*Eshelby*, 1957, eq. 5.7]:

$$\pm D(r) = \frac{\Delta\sigma}{\mu}\frac{4(2-\nu)}{\pi(1-\nu)} R\sqrt{1-\frac{r^2}{R^2}} = \frac{1}{2}\Delta D(r) \quad (1)$$

where D is the particle displacement on either side of the fault and ΔD is the displacement discontinuity (slip) across the fault at each point r, $\Delta\sigma$ is the stress drop, μ is the elastic shear modulus of the medium and ν the Poisson ratio. The model assumes a constant stress drop on a circular fault of radius R in a linear elastic whole space. The expression for $\Delta\sigma$ of an earthquake given the average slip $\Delta\bar{D}$ across the fault and assuming a Poisson solid ($\nu = 0.25$) is [e.g., *Keilis Borok*, 1959; *Kanamori and Anderson*, 1975]:

$$\Delta\sigma = \frac{7\pi}{16}\mu\frac{\Delta\bar{D}}{R}. \quad (2)$$

The assumption of a Poisson solid is a good approximation for granodiorite based on laboratory tests [*Gercek*, 2007]. Using this relationship, a shear modulus of μ = 30GPa, average slip $\Delta\bar{D} \approx$ 2.1 cm, and radius R = 5.75 m (Table 1) the coseismic static stress drop on the BCMF is approximately $\Delta\sigma \approx$ 150 MPa. A similar calculation based on the UHF yields a stress drop of 130 MPa. These are large stress drop values relative to the expected range 0.1 to 100 MPa. Before we discuss the implications of these findings, we first analyze potential sources of error in the analysis.

Discussion

Uncertainty and Analysis Limitations

Here we identify and attempt to quantify the sources of error for the stress drops calculated in the previous section. Possible sources of error are divided into two groups: (1) assumption of the source geometry (2) differentiation between seismic and aseismic slip; and (3) measurement of slip. The calculated stress drops for the BCMF and the UHF are summarized in Table 1.

(1) Source Dimensions

Eshelby's general solution for slip on an elliptical crack with aspect ratio *a/b* on which slip is parallel to the *a* axis is given by:

$$\pm D(x,y) = \frac{b\Delta\sigma}{C_1\mu}\sqrt{1-\frac{x^2}{a^2}-\frac{y^2}{b^2}} = \frac{1}{2}\Delta D(x,y) \tag{3}$$

This is the more general form of eq. (1) in Cartesian coordinates where slip is parallel to the *x*-axis. The coefficient C_1 is a function of the aspect ratio of the elliptical fault geometry and is given by *Eshelby* [1957, eq. 5.3]:

$$\begin{aligned} C_1 &= E(k) + \frac{\nu}{1-\nu}\frac{K(k)-E(k)}{k^2}; & a>b, k=\sqrt{1-b^2/a^2} \\ &= \frac{b}{a}\left[E(k)+\frac{\nu}{1-\nu}\frac{K(k)-a^2/b^2\,E(k)}{k^2}\right]; & b>a, k=\sqrt{1-a^2/b^2} \\ &= \frac{\pi(2-\nu)}{4(1-\nu)}; & a=b \end{aligned} \tag{4}$$

Here *E(k)* and *K(k)* are complete elliptical integrals of the first and second kind respectively. *Madariaga* [1977] evaluated similar expressions for the stress drop in terms of the *average* slip, $\Delta\bar{D}$:

$$\Delta\sigma = \frac{\mu}{C_2}\frac{\Delta\bar{D}}{W} \tag{5}$$

Where W is the shortest principal axis of the fault model (i.e. $W=R$ for the circular fault). For the circular ('penny-shaped') fault the commonly cited result for the coefficient C_2 is 16/7π [e.g., *Kanamori and Anderson*, 1975]. C_2 can be calculated for elliptical model faults of a variety of aspect ratios using [*Madariaga*, 1977]:

$$\begin{aligned} C_2 &= 4\left[3E(k) + \frac{K(k) - b^2/a^2\,E(k)}{k^2}\right]^{-1}; \quad a > b, k = \sqrt{1 - b^2/a^2} \\ &= 4\left[3E(k) + \frac{a^2}{b^2}\frac{K(k) - E(k)}{k^2}\right]^{-1}; \quad b > a, k = \sqrt{1 - a^2/b^2} \end{aligned} \tag{6}$$

In calculating the stress drop, we previously made the simplifying assumptions that (i) the fault mapped in two dimensions with measured half length R_a can be represented in three dimension by a circular fault; and (ii) that the radius R of the fault is equivalent to the measured half length R_a. Below we assess the net effect of each of these assumptions.

First, we keep the assumption that the fault is circular, but we relax the assumption that the apparent radius R_a exposed at the earth's surface is equal to the actual radius R of the crack. Let the line A-B (Figure 6A) be the intersection of the circular fault with the Earth's surface. Because the slip maximum according to eq. 1 occurs at the center of the fault ($r=R$), the stress drop can be expressed as a function of the maximum slip, ΔD_{max}:

$$\Delta\sigma = C_1\mu\frac{\Delta D_{\max}}{R} \tag{7}$$

With no knowledge of the actual size, using the apparent radius R_a and the maximum apparent slip D_a measured at point *m*, an apparent stress drop $\Delta\sigma_a$ is obtained:

$$\Delta\sigma_a = C_1 \mu \frac{\Delta D_a}{R_a} \quad (8)$$

However, according to Figure 6A we may replace $r = R \sin\theta$ in eq. 1 to obtain:

$$D(r) = \frac{\Delta\sigma}{C_1\mu} R\sqrt{1-\sin^2\theta} \quad (9)$$

and using the fact that $R_a = R\cos\theta$ we obtain:.

$$\Delta\sigma_a = \frac{\Delta\sigma\sqrt{1-\sin^2\theta}}{\cos\theta} = \Delta\sigma \quad . \quad (10)$$

In conclusion, the ratio D_a/R_a remains identical to *D/R*; as a consequence, measurement of apparent maximum slip and radius along any arbitrary section of a circular model fault yields the correct stress drop estimate through eq. (3). The same observations apply when using average apparent slip, instead of the maximum apparent slip: the correct scaling with stress drop is maintained through any section of the model fault. It can also be shown that the apparent half length, *a*, of any elliptical fault scales linearly with slip.

If the assumption that the crack is circular is dropped, and the possibility is considered that the fault may approximate an ellipse, the resulting stress drop will vary depending on the aspect ratio of the fault and the length of the semi-minor axis. We can calculate the stress drop for elliptical faults using eq. (5) and (6). If we assume that a reasonable range of elliptical fault aspect ratios is in the range $0.5 \leq a/b \leq 2$, then we can calculate the range of possible stress drops represented by two dimensional fault exposures. Faults of aspect ratios less than one, on which the slip direction is parallel to the semi-minor axis (Figure 6B), were called 'transversal slip' faults by *Madariaga* [1977] while faults with aspect ratios greater than one, on which slip is parallel to the semi-major axis, were classified as 'longitudinal slip' faults (Figure 6C). If the BCMF is a transversal slip fault with an aspect ratio equal to 0.5, the corresponding stress drop is reduced to $\Delta\sigma \approx 110$MPa. Assuming the BCMF is a longitudinal slip fault with an aspect ratio equal to 2 implies that the semi-minor axis is vertical, and the apparent length of the semi-minor axis is half the measured length of the fault in the field. Correspondingly, using the value W=b=3m, and the appropriate expression from eq. (6), the corresponding stress drop is $\Delta\sigma \approx 250$ MPa. Thus, taking into account the geometric error introduced by extrapolating the two dimensional map to three dimensions extends the range of possible stress drop values to 110 MPa $\leq \Delta\sigma \leq$ 250 MPa. Similar estimates for the stress drop on the UHF yield stress drops of 90 MPa $\leq \Delta\sigma \leq$ 230 MPa.

(2) Differentiation between seismic and aseismic slip

Ultimately, stress drop and slip under brittle conditions should not be very different whether they occurred quasi-statically or seismically. Due to dynamic overshoot, slip (and stress drop, may be as much as 30% larger during seismic slip [*Madariaga*, 1976]. The recognition of seismic slip from outcrop observations along faults remains a difficult and controversial topic [e.g., *Cowan*, 1999]. We argue that the slip recorded by rhombochasms may have been seismic based on two lines of evidence: i) textures within the opening rhombochasms suggest that the associated slip was nearly instantaneous. These textures include randomly oriented epidote grains in all rhombochasms as well as implosion breccias. The fact that these textures show no post-formation shearing disruption suggest that they formed in a single event. (ii) Thin (<1mm) pseudotachylyte veins are found on nearby Bear Creek faults [*Griffith et al.*, 2008]. These observations support the interpretation that brittle slip along these faults was seismic.

(3) Measurement of slip

Here we present a kinematic model for the rhombochasm formation (Figure 7) to justify in more detail our assumption that the length of the rhombochasm represents the magnitude of slip in a single event. The faulting begins as a tabular quartz mylonite with distributed crystal-plastic shearing across its thickness and bounded on either side by granodiorite (Figure 7i). Shearing across the quartz mylonite involves no slip at the mylonite-granodiorite interfaces. Subsequently, more localized brittle shearing develops at the interfaces forming cataclasite slip zones in a left stepping configuration (Figure 7ii). A small amount of localized shearing continues until the tensile strength of the quartz mylonite in the relay zone is exceeded [e.g., *Segall and Pollard*, 1980; *Martel and Pollard*, 1989; *Mutlu and Pollard*, 2008], and a tensile opening fracture forms, linking the two cataclastic slip zones (Figure 7iii). This linking fracture cuts the cataclastic slip zones into short, abandoned, non-shearing zones including the tips, and actively shearing echelon zones on either side of the tabular quartz mylonite. As slip progresses in the echelon cataclastic zones, deformation in the quartz mylonite is primarily ascribed to opening of the rhombochasm (Figure 7iv). On the interface between the granodiorite and rhombochasm interior, there is no new cataclasite generation, thus cataclasite thins from the actively slipping zone to the distal edge of the rhombochasm. As slip progresses, thin cataclasite far from the actively shearing zone is spalled into the rhombochasm and/or dissolved as fluids are sucked into the rhombochasm from the adjacent granodiorite (Figure 7v). As shearing ceases, within the rhombochasm only the portion of the cataclastic zone closest to the actively shearing cataclasite zone if any at all is preserved. Epidote is precipitated and fills the rhombochasm with euhedral, randomly oriented crystals. In this model, the length of the rhombochasm should approximate the magnitude of slip, ΔD, of a single slipping event.

We note that a small amount of underestimation is introduced by assumption that this process can be approximated by the kinematic block model summarized above. In Figure 7iii, a small amount of slip must accumulate along the cataclastic zones before the tensile strength in the relay zone is exceeded [e.g. Segall and Pollard, 1980]. This slip is not recorded by the rhombochasm opening; however we expect the amount of slip necessary to breach the relay zone to be very small relative to the rhombochasm length. Also of note is that average measured rhombochasm length measured on the Bear Creek faults is approximately 2 cm, within the range of single slip values estimated for nearby pseudotachylyte-bearing faults based on conductive heat transfer calculations [*Griffith et al*., 2008].

Stress Drop Implications

The stress drops estimated here are large relative to the majority of data available in the seismological literature [e.g., *Abercrombie*, 1995]; however they are not without precedent. Stress drops on the order of hundreds of MPa appear to be rare, but have been observed using seismology [*Kanamori*, 1994]. *Munguia and Brune* [1984] calculated stress drops in excess of 200 MPa for events in the Victoria, Baja California earthquake swarm of 1978. *Kanamori et al* [, 1990; 1993] estimated stress drops for a small earthquake in Pasadena, CA between 30 and 200 MPa. *Imanishi and Ellsworth* [2006] studied 34 M-0.2-M2.1 earthquakes near Parkfield, CA from the SAFOD Pilot Hole Array and found that half had stress drops greater than 10 MPa, with some exceeding 50 MPa. *Nadeau and Johnson* [1998] estimated stress drops on the order of 100 MPa and greater for repeating micro-earthquakes near Parkfield. They found that stress drops increased with decreasing seismic moment up to $\Delta\sigma \approx$ 2000 MPa for the smallest earthquakes (W≈0.5) [*Nadeau and Johnson*, 1998]. This is approximately the lattice shear strength of an asperity in granitoid rocks with no unhealed flaws [*Sammis et al*., 2001].

Stress drops calculated using values from field mapping of the BCMF and UHF are in the range 90 MPa ≤ $\Delta\sigma \leq$ 250 MPa considering a range of three dimensional source geometries. These values are near the upper bound of scaling relationships based on the bulk of seismological data available [*Kanamori*, 1994; *Abercrombie*, 1995], yet they lie within observed ranges of microearthquakes near Parkfield. Because they are on the order of hundreds of MPa, we suggest that these were "strong" faults as defined by *Kanamori* [1994].

The interpretation that the Bear Creek faults represent "strong" faults is consistent with interpretations regarding observations of pseudotachylyte-bearing faults in other locations [e.g., *Di Toro and Pennacchioni*, 2005; *Sibson and Toy*, 2006]. Our observations indicate that the stress drop associated with earthquake ruptures along these faults represent a large percentage of total fault strength. The reason for this may lie in the nature of the interface on which the slip events occurred. All of the brittle slip that took place on the rhombochasm-bearing faults occurred on the interface between mylonitized quartz veins and the adjacent host granodiorite. This interface may have represented an at least partially healed asperity, stronger than a typical frictional fault, yet weaker than the surrounding undamaged granodiorite such that flaws concentrated and grew along the quartz mylonite-granodiorite interface.

Conclusions

Using detailed mapping of small faults in the Bear Creek drainage of the central Sierra Nevada, we estimate coseismic stress drops for ancient earthquakes using rhombochasms as slip markers. This method constrains, with high resolution in two dimensions, the source dimensions of ancient brittle slip events. Errors introduced in the stress drop calculations by inferring the three dimensional fault geometry from the mapped geometry is approximately a factor of two. The total range of possible stress drops is 90 MPa ≤ $\Delta\sigma \leq$ 250 MPa. This is larger than typical estimates for small earthquakes, and at the upper limit of self-similar scaling laws for all earthquakes. Therefore we suggest that faults of the Bear Creek area were strong faults, and earthquakes along these faults represented static stress drops that were a large fraction of the total fault strength.

References

Abercrombie, R. E. (1995), Earthquake source scaling relationships from -1 to 5 ML using seismograms recorded at 2.5-km depth, *J. Geophys. Res*., *100*, 24015-24036.

Ague, J. J. and G. H. Brimhall (1988), Magmatic arc aysymmetry and distribution of anomalous plutonic belts in the batholiths of California: effects of assimilation, crustal thickness, and depth of crystallization, Geol. *Soc. Am. Bull., 100,* 912-927.

Aki, K. (1967), Scaling law of seismic spectrum,*Bull. Seismol. Soc. Am., 72*, 1217-1231.

Anderson, J. G. and S. Hough (1984), A model for the shape of the Fourier amplitude spectrum of acceleration at high frequencies, *Bull. Seismol. Soc. Am., 74,* 1969-1994.

Archuleta, R. J., E. Cranswick C. Mueller, and P. Spudich (1982), Source parameters of the 1980 Mammoth Lakes, California, earthquake sequence, *J. Geophys. Res., 87*, 4595-4607.

Bergbauer, S. and S. J. Martel (1999). Formation of joints in cooling plutons, *J. Struct. Geol., 21*(7), 821-835.

Brace, W. F. and J. Byerlee (1966), Stick-slip as a mechanism for earthquakes, *153*, 990-992.

Burgmann, R., D. D. Pollard, S. J. Martel (1994), Slip distributions on faults; effects of stress gradients, inelastic deformation, heterogeneous host-rock stiffness, and fault interaction, *J. Struct. Geol., 16*(12), 1,675-1,690.

Cowan, D. (1999), Do faults preserve a record of seismic slip?-a field geologist's opinion, *J. Struct. Geol., 21*, 2703-2719.

Cowie, P. A. and C. H. Scholz (1992), Physical explanation for the displacement-length relationships of faults, using a post-yield fracture mechanics model, *J. Struct. Geol., 14*, 1133-1148.

Di Toro, G., G. Pennacchioni, G. Teza (2005), Can pseudotachylytes be used to infer earthquake source parameters? An example of limitations in the study of exhumed faults, *402*, 3-20.

Di Toro, G. and G. Pennacchioni (2005), Fault plane processes and mesoscopic structure of a strong-type seismogenic fault in tonalites (Adamello batholith, Southern Italian Alps), *Tectonophysics*, *402,* 55-80.

Eshelby, J. D. (1957), The determination of the elastic field of an ellipsoidal inclusion and related problems, *Proc. Royal Soc. Lon., A241*, 376-396.

Gercek, H. (2007), Poisson's ratio values for rock, *Int. J. Rock Mech. Min. Sci., 44*, 1-13.

Griffith, W. A., G. Di Toro, G. Pennacchioni, D. Pollard (2008), Thin Pseudotachylytes in Faults of the Mt. Abbot Quadrangle, Sierra Nevada California: Physical Constraints on Seismic Slip, *J. Struct. Geol*, in press.

Guo, H. A., A. Lerner-Lam, S. E. Hough (1992), Emperical Green's function study of Loma Prieta aftershocks: Evidence for fault zone complexity, *Seismol. Res. Lett*., *63,* 76.

Hanks, T. C. (1982), f_{max}, *Bull. Seismol. Soc. Am. ,71*, 1867-1879.

Hough, S. E. and J. G. Anderson (1988), High frequency spectra observed at Anza, California:

Implications for Q structure, *Bull. Seismol. Soc. Am., 78,* 692-707.

Ide, S. and G. Beroza (2001), Does apparent stress vary with earthquake size?, *Geophys. Res. Lett*., *28*, 3349-3352.

Imanishi, K. and W. L. Ellsworth, (2006), Source scaling relationships of microearthquakes at Parkfield, CA, determined using the SAFOD pilot hole seismic array. Radiated Energy and the Physics of Earthquake Faulting, *American Geophysical Union Monograph.*

Kanamori, H. and D. L. Anderson (1975). Theoretical basis of some empirical relations in seismology, *Bull. Seismol. Soc. Am., 65*, 1073-1095.

Kanamori, H., J. Mori, T. H. Heaton (1990), The 3 December 1988, Pasadena Earthquake (ML=4.9) recorded with the very broadband system in Pasadena, *Bull. Seismol. Soc. Am.*, *80,* 483-487.

Kanamori, H., J. Mori, E. Hauksson, T. H. Heaton, L. K. Hutton, and L.M. Jones (1993), Determination of earthquake energy release and ML using TERRAscope, *Bull. Seismol. Soc. Am.*, 2, 330-346.

Kanamori, H. (1994), Mechanics of earthquakes, *Annu. Rev. Earth Planet. Sci., 22*, 207-237.

Kattenhorn, S. A. and D. D. Pollard (2001), Integrating 3D sismic data, field analogs and mechanical models in the analysis of segmented normal faults in the Wytch Farm oilfield, southern England , *AAPG Bulletin, 85*, 1183-1210.

Keilis-Borok, V. I. (1959), On the estimation of the displacement in an earthquake source and of source dimensions, *Ann. Geophis., 12*, 205-214.

Lockwood, J. P. and P. A. Lydon (1975), U. S. Geologic map of the Mount Abbot quadrangle, California. scale 1:62,500.

Madariaga, R. (1976), Dynamics of an expanding circular fault, *Bull. Seismol. Soc. Am., 66*(3), 639-666.

Madariaga, R. (1977), Implications of Stress-Drop Models of Earthquakes for the Inversion of Stress Drop From Seismic Observations, *Pageoph.,115*, 301-315.

Maerten, L. and D. D. Pollard (2001), Three-dimensional digital field mapping of the Chimney Rock fault system, central Utah, *J. Struct. Geol, 23*, 585-592.

Magloughlin, J. F. (1992), Microstructural and chemical changes associated with cataclasis and frictional melting at shallow crustal levels: the cataclasite-pseudotachylyte connection, *Tectonophysics*, 204, 243-260.

Manighetti, I., G. C. P. King, Y. Gaudemer, C. H.. Scholz, and C. Doubre (2001). Slip accumulation and lateral propagation of active normal faults in Afar, *J. Geophys. Res.*, *106*, 13667-13696.

Martel, S. J., D. D. Pollard, and P. Segall (1988), Development of simple strike-slip fault zones, Mount Abbot Quadrangle, Sierra Nevada, California, *Geol. Soc. Am. Bull., 100*, 1,451-1,465.

Munguia, L. and J. N. Brune (1984), High stress drop events in the Victoria, Baja California earthquake swarm of 1978, *Geophys. J. R. Astr. Soc*., *76*, 725-752.

Mutlu, O., and D. D. Pollard (2008), On the patterns of wing cracks along an outcrop scale flaw: a numerical modeling approach using complementarity: *Journal of Geophysical Research, 113*, doi:10.1029/2007JB005284.

Nadeau, R. M. and L. R. Johnson (1998), Seismological studies at Parkfield VI: Moment release rates and estimates of source parameters for small repeating earthquakes, *Bull. Seismol. Soc. Am.*, *88*, 790-814.

Prejean, S. G. and W. L. Ellsworth (2001), Observations of earthquake source parameters at 2km depth in the Long Valley Caldera, Eastern California, *Bull. Seismol. Soc. Am.*, *91*, 165-177.

Ramsay, J. G. (1980), The crack-seal mechanism of rock deformation, *Nature*, 284, 135-139.

Richardson, E. and T. H. Jordan (2002), Seismicity in deep gold mines of South Africa: Implications for tectonic earthquakes, *Bull. Seismol. Soc. Am.*, *92*, 1766-1782.

Rudnicki, J. W. (1980), Fracture mechanics applied to the earth's crust, *Ann. Rev. Earth. Plan. Sci.*, *8*, 489-525.

Sammis, C. G., R. M. Nadeau, and L.R. Johnson (2001), How strong is an asperity?, *J. Geophys. Res*. *104*(B5), 10,609-10,619.

Scholz, C. H. (2002), *The Mechanics of Earthquakes and Faulting.* Cambridge, Cambridge University Press, 471p.

Segall, P. and D. D. Pollard (1980), Mechanics of discontinuous faults., *J. Geophys. Res*., *85*: 4,337-4,350.

Segall, P. and D. D. Pollard (1983), Nucleation and growth of strike slip faults in granite, *J. Geophys. Res*., *88*, 555-568.

Segall, P. and D. D. Pollard (1983), Joint formation in granitic rock of the Sierra Nevada, *Geol. Soc. Am. Bull*., *94*, 563-575.

Segall, P., E. H. McKee, S. J. Martel, B. D. Turrin (1990), Late Cretaceous age of fractures in the Sierra Nevada batholith, California, *Geology*, *18*, 1,248-1,251.

Sharp, W. E. (1965). The deposition of hydrothermal quartz and calcite, *Economic Geology*, *60*, 1635-1644.

Shipton, Z. K., A. K. Soden, J. P. Kirkpatrick, A.M. Bright, R.J. Lunn, (2006), How thick is a fault? Fault displacement-thickness scaling revisited, *Radiated Energy and the Physics of Earthquake Faulting*, American Geophysical Union Monograph.

Sibson, R. H. (1975), Generation of pseudotachylyte by ancient seismic faulting, *Geophys. J. R. Ast. Soc.*, *43*, 775-794.

Sibson, R. H. (1985), Stopping of earthquake ruptures at dilational fault jogs, *Nature*, *316*, 248-251.

Sibson, R. H. (1986), Brecciation processes in fault zones: Inferences from earthquake rupturing, *Pageoph*, 124, 159-175.

Sibson, R. H. and V. G. Toy (2006), The habitat of fault-generated pseudotachylyte: Presence vs. absence of Friction-Melt. Earthquakes: Radiated Energy and The Physics of Faulting. R. E. Abercrombie, A. McGarr, H. Kanamori and G. Di Toro, American Geophysical Union.

Stern, T. W., P. C. Bateman, et al. (1981), Isotopic U-Pb ages of zircon from the granitoids of the central Sierra Nevada, California, 1185, 17.

Willemse, E. J. M. (1997), Segmented normal faults; correspondence between three-dimensional mechanical models and field data, *J. Geophys. Res.*, *102*(1), 675-692.

Figure Captions

Figure 1: Conceptual model of macroscopic and microscopic evolution of faults in Bear Creek. I-III correspond to the macroscopic evolution of faults suggested by Martel et al (1988), where in stage I joints form in response to thermal stresses; stage II is marked by slip nucleation along

joints and subsequent linkage to form small faults; and in stage III simple fault zones composed of paired small faults linked by secondary fractures form due to interaction of neighbouring faults. Martel (1990) also proposed a fourth stage of development in which simple fault zones coalesce to form large, complex fault zones, but the fourth stage has been omitted from this figure for simplicity. Dashed circles in II and III indicate the location of A, B, C, and D. A-D represent the microstructural evolution of faults from the time that shearing commences to the transition from shearing deformation to zeolite veining. (A) Quartz precipitated in dilatational regions along faults is sheared at temperatures greater than 400^{o}C producing quartz mylonites. (B) Boundaries between mylonites and granodiorites are filled with epidote veins and reactivated by cataclasites cemented by epidote. Locally cataclasites and epidote veins cut across mylonites. (C) Thin, discontinuous pseudotachylyte veins form due to seismic slip, and locally cut mylonites and cataclasites. (D) The termination of shear deformation is signified by opening of faults and zeolite mineralization.

Figure 2: Field photographs (left side) and schematic drawings (right side) of three different types of epidote-filled dilational jogs found along Bear Creek faults. (A) A releasing bend in a fault. (B) A dilational stepover between two small faults. (C) A dilational stepover between two cataclastic slip surfaces localized on the boundary between tabular quartz mylonites and host granodiorite. The configurations shown in B and C produce rhombohedron-shaped openings (rhombochasms) which can be used as slip markers along the faults. Gray = granodiorite; green = epidote; white = quartz mylonite; and bleached/speckled = altered granodiorite.

Figure 3: Trace maps of rhombochasm-bearing faults. (BCMF) Bear Creek Meadows Fault;. (UHF) Upper Hilgard Meadows Fault with segments 1 and 2 from Figure 5B; (LHF); Lower Hilgard Meadows Fault; (BJF) Big Juniper Fault.

Figure 4: Rhombocham microstructures. (A) Field photograph of rhombochasm pictured in B. (B) Photomosaic of a rhombochasm on the Bear Creek Meadows Rhomb Fault (Fig. 3, BCMF) (optical photomicrograph, plane polarized light). (C) Epidote crystals and quartz grains from Lower Hilgard Meadows Fault (Figure. 3, LHF) (optical photomicrograph, plane polarized light). (D) Dark vein penetrating into the rhombochasm from BCMF (see Figure 4G). This vein is part of the slip zone extending into the rhombochasm, and has some identifying characteristics of pseudotachylyte (injection vein, aphanitic, optically cloudy), but upon closer inspection consists of ultrafine-grained epidote. The dark vein is truncated by a later zeolite-bearing vein (optical photomicrograph, plane polarized light). (E) Contact between rhombochasm filling and granodiorite. No evidence of slip is preserved along this contact (SEM backscattered electron image). (F) The ~0.2-0.4 mm thick slip zone separating rhombochasm filling and granodiorite (SEM backscattered electron image). Images E and F were taken along the same (upper "slip zone"??) rhombochasm-granodiorite contact from fault BCM. (G) Slip zone along the BCMF which does not penetrate into the rhombochasm. Note that fabric formed by epidotes is seamless between the rhombochasm and the slip zone. Image is taken from a rhombochasm several centimeters from the rhombochasm from Figure 4 E & F along the BCMF.

Figure 5: Slip distributions along (A) the Bear Creek Meadows Rhomb Fault (BCMF) and (B) the Upper Hilgard Rhomb Fault (UHF), as determined by measuring the length of rhombochasms (brittle slip) and dike offset (ductile slip).

Figure 6: Constant stress dropped models for elliptical faults with aspect ratios (*a/b*) varying from 0.5 to 2. For each model, the upper diagram shows the coordinate system and the hypothetical erosional surface exposed in outcrop is shown by the line A-B. The lower plot in each diagram shows predicted slip distributions for a given constant stress drop. Note that the horizontal axis *a* is equal in all plots. Only the unknown *b* axis varies in each plot. (A) Penny shaped-crack model (*a/b*=1). (B) Transversal slip fault (*a*<*b*). (C) Longitudinal slip fault (a>b). See text for more detail.

Figure 7: Kinematic model for rhombochasm formation where stages in (A) indicate the steps of rhombocasm initiation and (B) and (C) illustrate possible stages during the rhombochasm evolution. See text for complete discussion.

Tables

Table 1: Summary of Fault Source Parameters

Fault	W (m)	a/b	ΔD_{ave} (cm)	ΔD_{max} (cm)	Dike offset (cm)	$\Delta\sigma$ (MPa)
BCMF	5.75	1	0.8-2.1	4.5	35	150
BCMF	5.75	0.5	0.8-2.1	4.5	35	110
BCMF	2.88	2	0.8-2.1	4.5	35	250
UHF	6.25	1	0.8-2.0	3.6	42	130
UHF	6.25	0.5	0.8-2.0	3.6	42	90
UHF	3.13	2	0.8-2.0	3.6	42	*220*
LHF	-	-	2.6	5.1	14	-
BJF	-	-	1.2	2.6	4.8	-

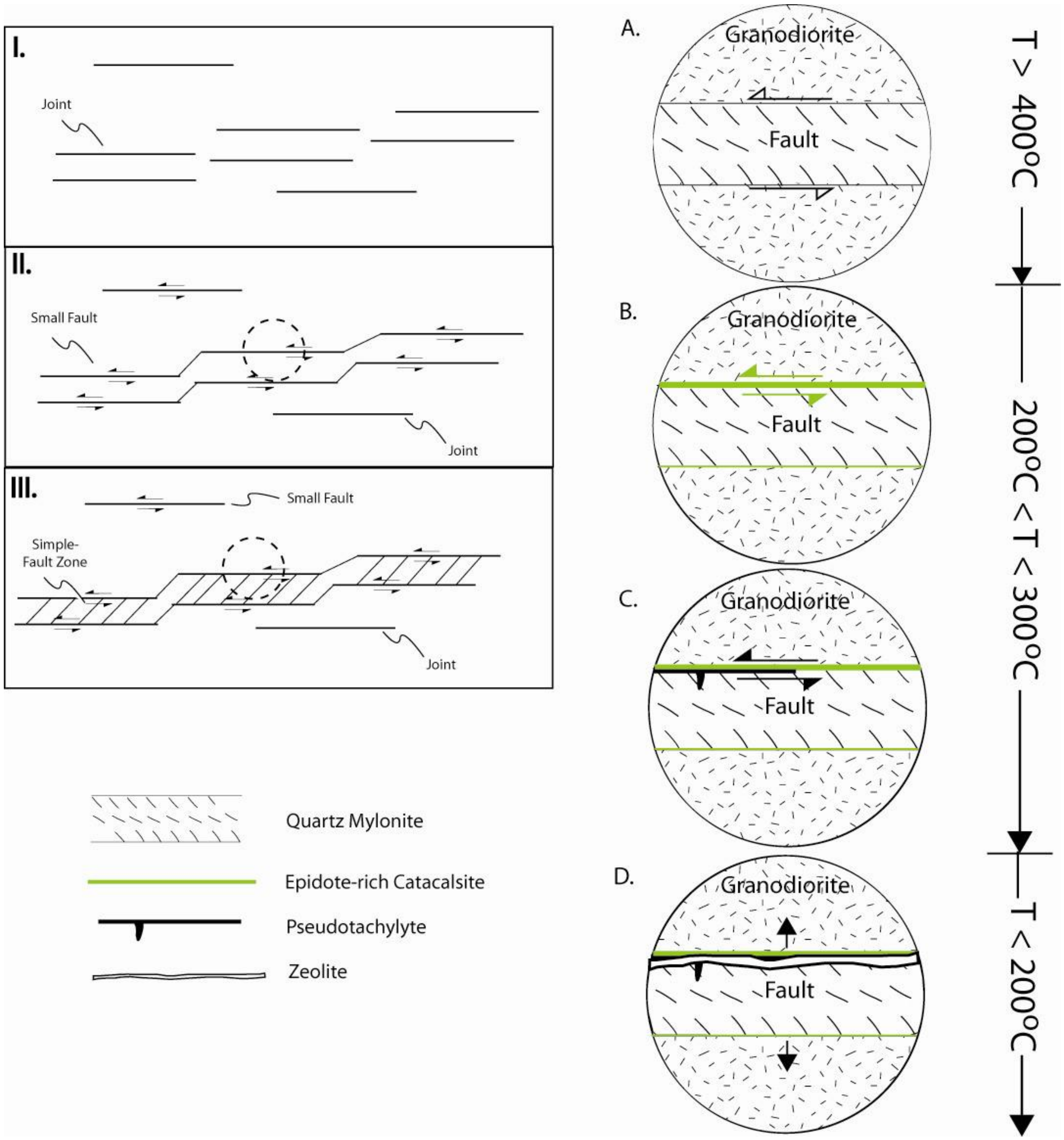
I.
Joint
II.
Small Fault
Joint
III.
Small Fault
Simple-
Fault Zone
Joint
Quartz Mylonite
Epidote-rich Catacalsite
Pseudotachylyte
Zeolite
A.
Granodiorite
Fault
B.
Granodiorite
Fault
C.
Granodiorite
Fault
D.
Granodiorite
Fault
T > 400°C
200°C < T < 300°C
T < 200°C

Figure 1

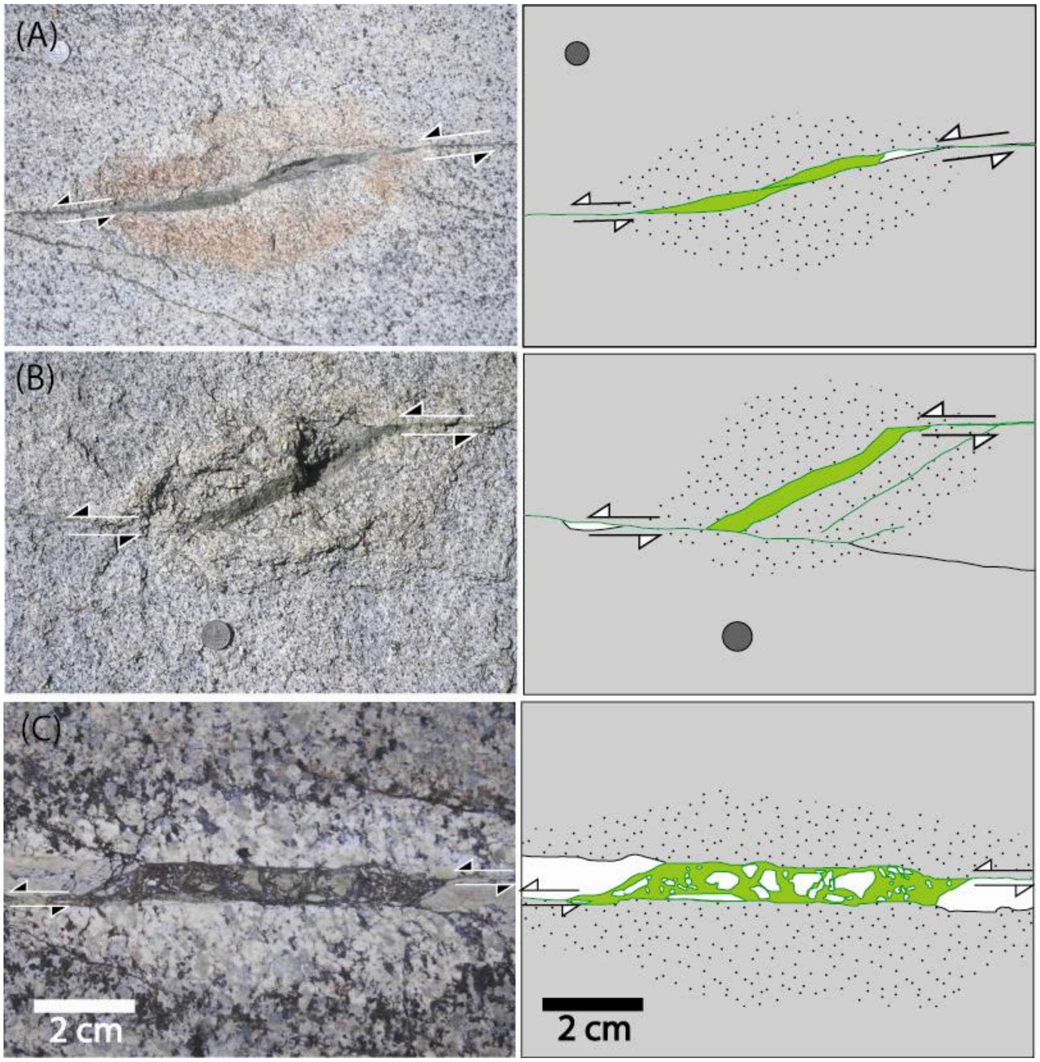

Figure 2

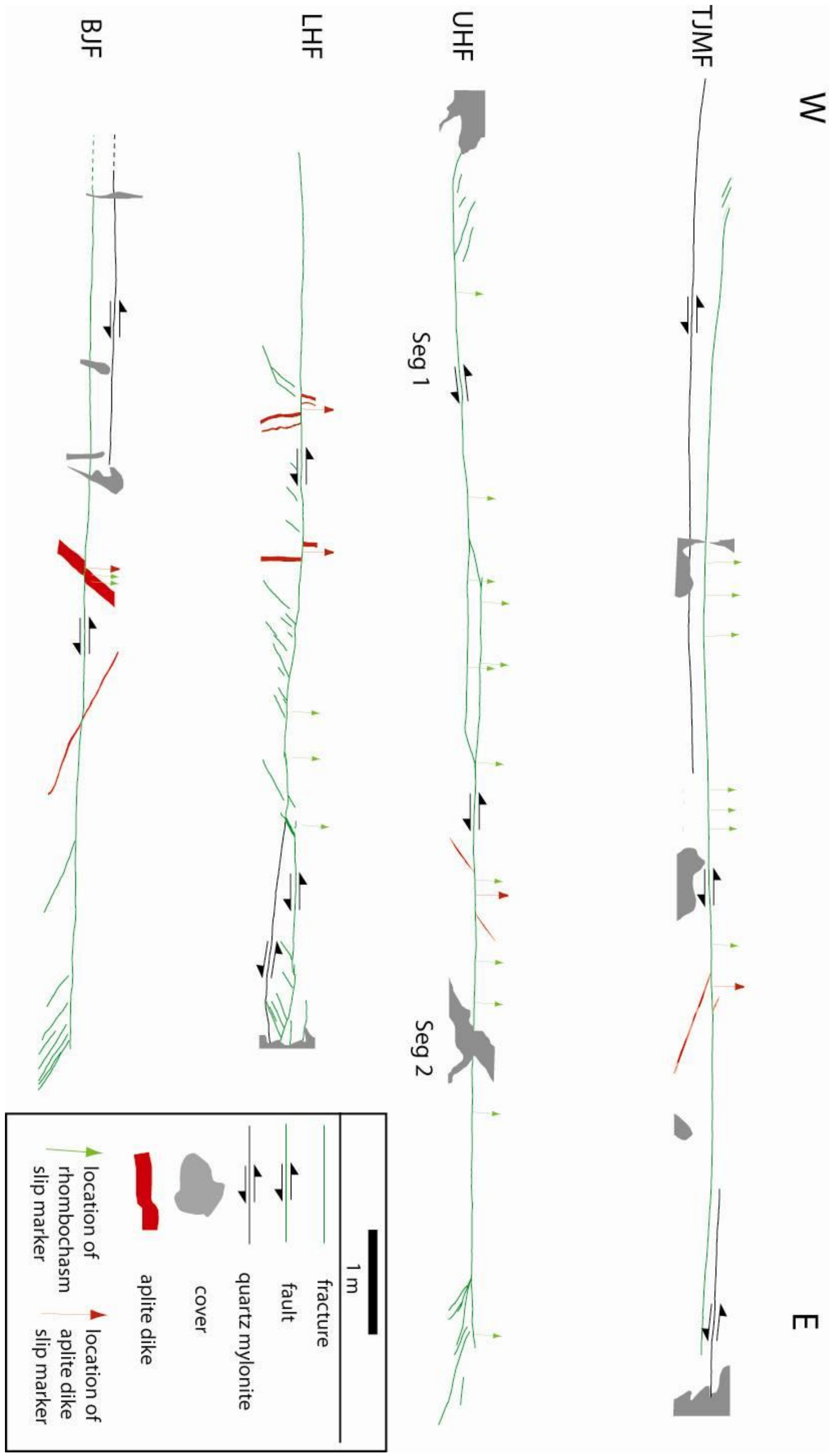
W
E
TJMF
UHF
LHF
BJF
Seg 1
Seg 2
1 m
fracture
fault
quartz mylonite
cover
aplite dike
location of rhombochasm slip marker
location of aplite dike slip marker

Figure 3

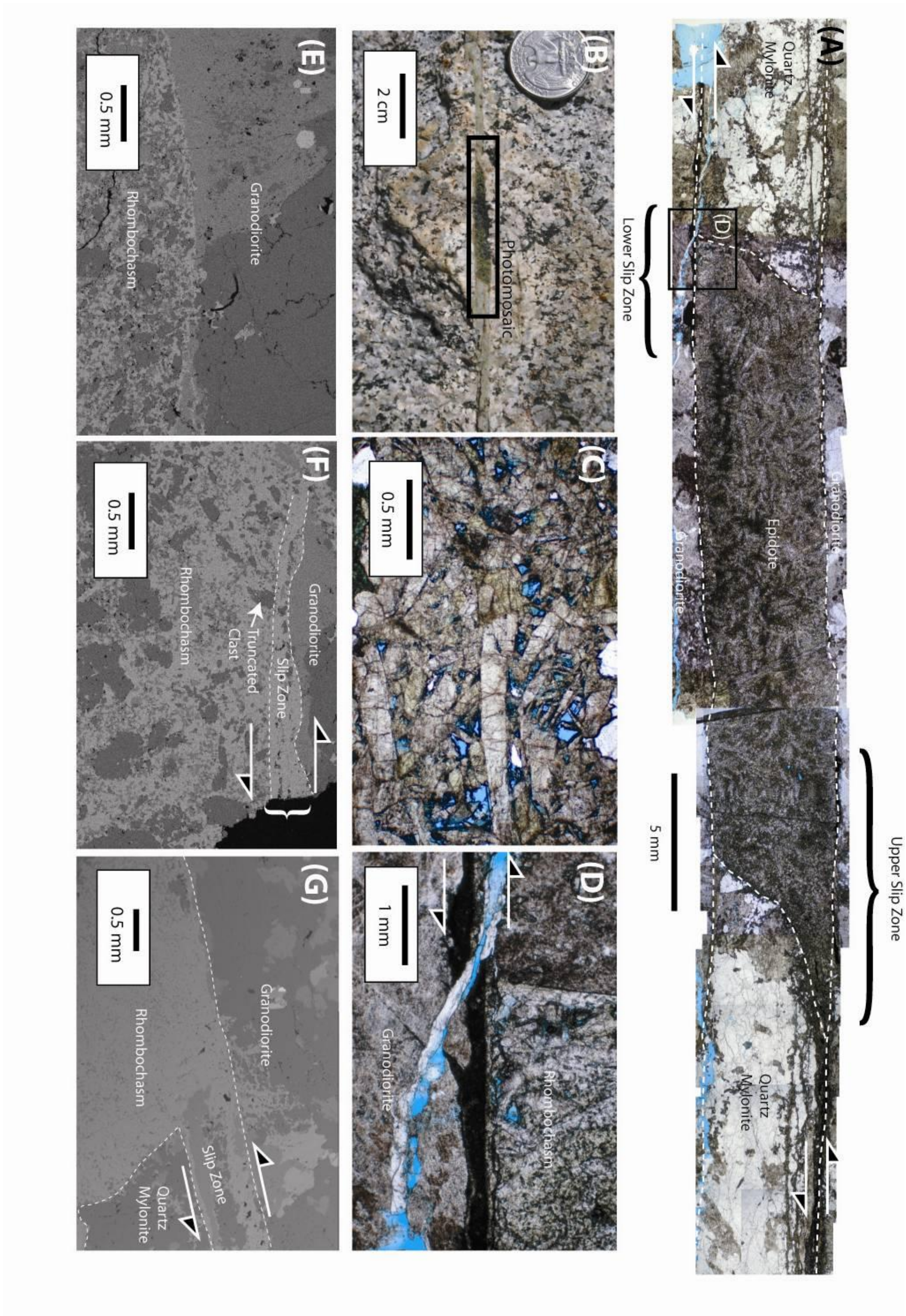
(A)
Quartz Mylonite
(D)
Lower Slip Zone
Granodiorite
Epidote
Granodiorite
Upper Slip Zone
5 mm
Quartz Mylonite
(B)
Photomosaic
2 cm
(C)
0.5 mm
(D)
1 mm
Rhombochasm
Granodiorite
(E)
0.5 mm
Granodiorite
Rhombochasm
(F)
0.5 mm
Granodiorite
Slip Zone
Truncated Clast
Rhombochasm
(G)
0.5 mm
Granodiorite
Rhombochasm
Slip Zone
Quartz Mylonite

Figure 4

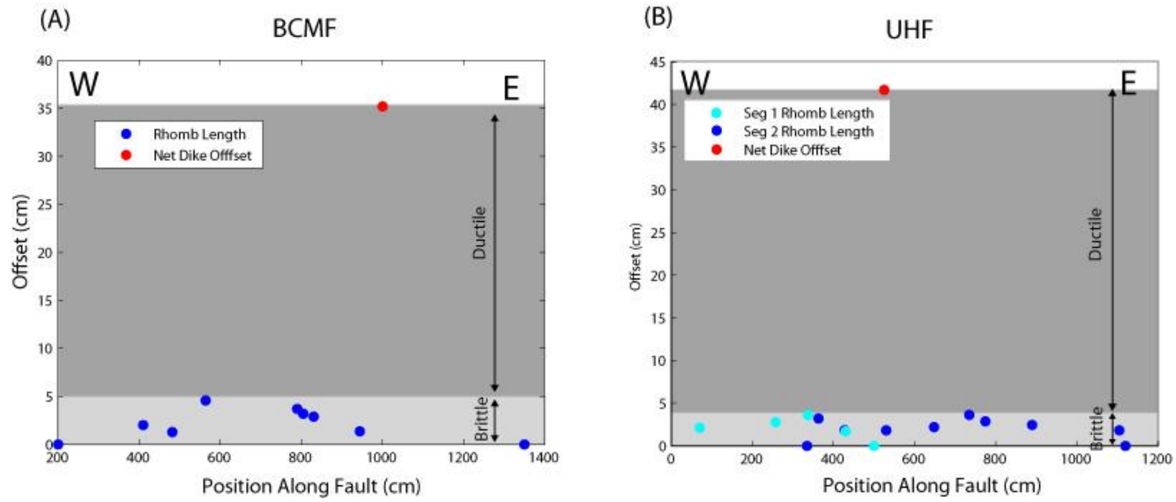

Figure 5

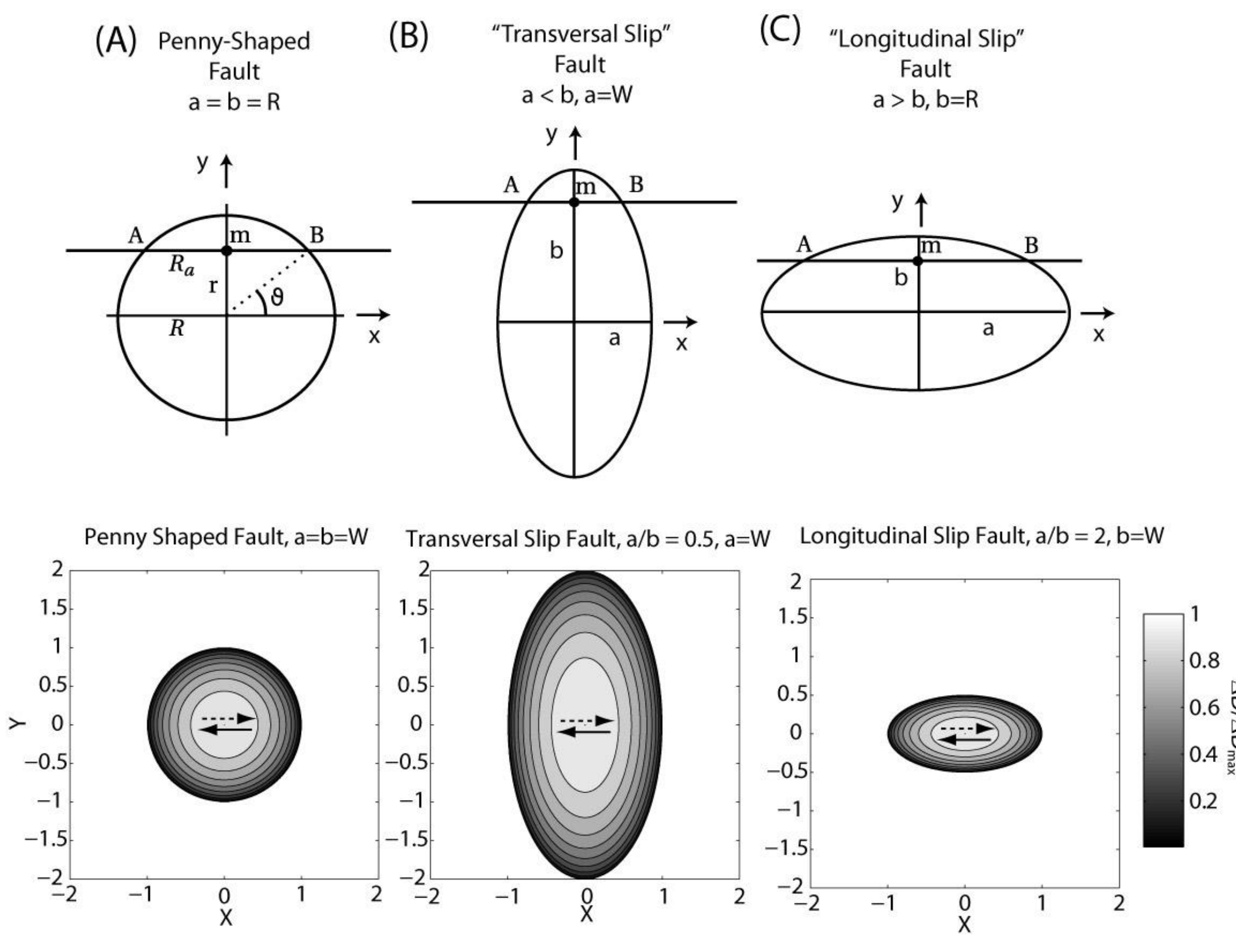

Figure 6

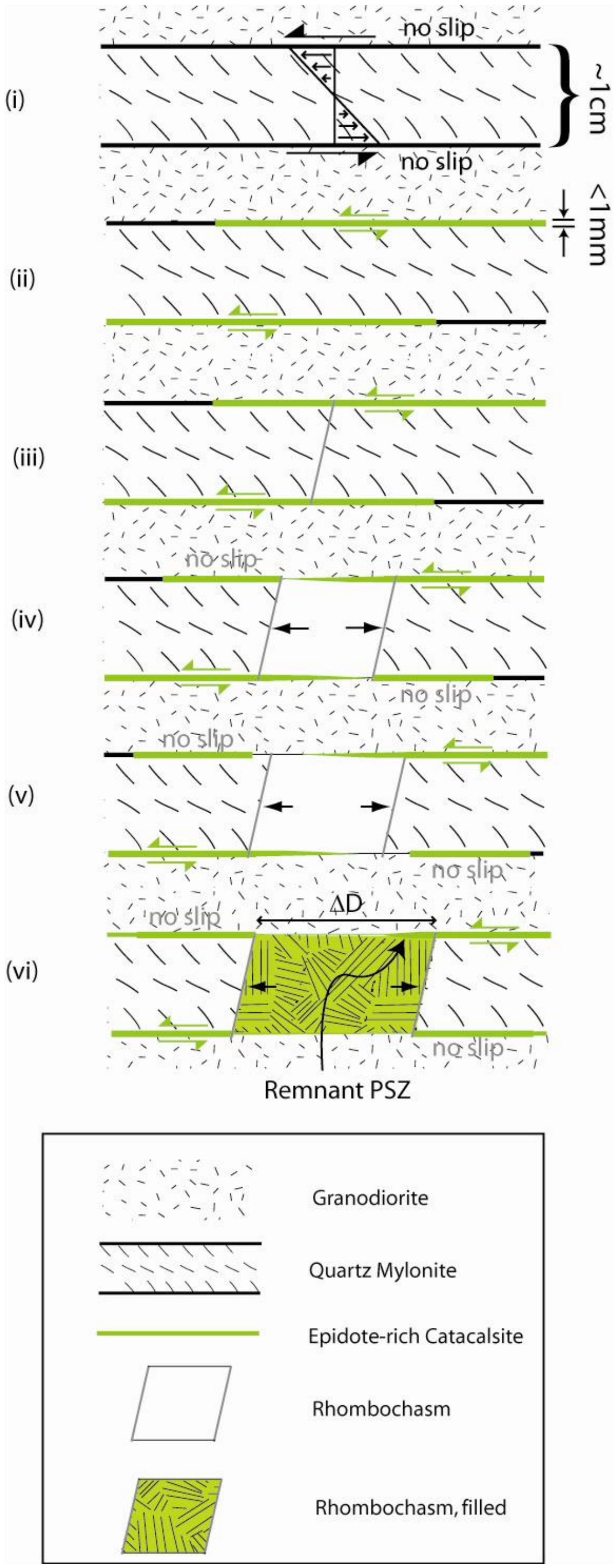

no slip
~1cm
(i)
no slip
<1mm
(ii)
(iii)
no slip
(iv)
no slip
no slip
(v)
no slip
ΔD
no slip
(vi)
no slip
Remnant PSZ
Granodiorite
Quartz Mylonite
Epidote-rich Catacalsite
Rhombochasm
Rhombochasm, filled

Figure 7